

NUMERICAL INVESTIGATION OF HVAF-SPRAYED Fe-BASED AMORPHOUS COATINGS

NUMERIČNE RAZISKAVE S POSTOPKOM HVAF NAPRŠENIH AMORFNIH PREVLEK NA OSNOVI ŽELEZA

Nianchu Wu*, Tingting Li, Jingbao Lian

Liaoning Petrochemical University, School of Mechanical Engineering, Fushun, China

Prejem rokopisa – received: 2022-09-29; sprejem za objavo – accepted for publication: 2022-10-25

doi:10.17222/mit.2022.636

A numerical analysis was performed to predict the effect of the convergent section geometry of a gun nozzle on the high-velocity air-fuel (HVAF) thermal spray Fe-based amorphous coating (AC) process. A computational fluid dynamics model was applied to investigate the gas-flow field and the behavior of in-flight particles at nozzle entrance convergent section length ranging from 28 mm to 56.8 mm and different shapes of the Laval nozzle convergent section (a straight line and Vitosinski convergence curve). On the one hand, the change in the gas-flame flow characteristics for the Vitosinski curve shows a uniform and stable flame compared with the straight-line curve in the convergent section. The straight-line curve shape of the Laval nozzle convergent section has a higher particle temperature compared with the Vitosinski-curve shape of the Laval nozzle convergent section. The particle dwell time for the straight-line curve shape of the Laval nozzle convergent section is longer than that for the Vitosinski curve shape of the Laval nozzle convergent section. On the other hand, the nozzle entrance convergent section length obviously affects the particle temperature, and the particle dwell time increases with the increasing nozzle entrance convergent section length. By analyzing both the melt status of the particles and particle velocity, the optimal gun configuration (0.7 V) producing low-porosity coatings was predicted. These calculations were experimentally verified by producing a low-porosity (1.37 %) Fe-based AC, fabricated with HVAF using the predicted optimal gun configuration.

Keywords: Fe-based amorphous coatings, high-velocity air fuel, computational simulation, nozzle

Numerična analiza je bila uporabljena za napoved učinka konvergentnega profila šobe na puški, uporabljeni pri postopku zelo hitrega termičnega naprševanja amorfne prevleke na osnovi železa s plinsko mešanico propan (C_3H_8)-zrak (HVAF; angl.: High-Velocity Air Fuel). Za raziskavo je bil uporabljen računalniški model na osnovi dinamike fluidov in obnašanje znotraj plinske mešanice letečih delcev na vhodu šobe s konvergentnim profilom dolžine od 28 mm do 56,8 mm in različno obliko konvergentnega dela Lavalove šobe (ravna linija in konvergenčna ukrivljenost po Vitosinskem). Sprememba pretoka plinske mešanice oziroma lastnosti plamena pri uporabi Vitosinske krivulje je pokazala enovit in stabilen plamen v primerjavi z uporabo ravne linije v konvergentnem delu šobe. Pri izbiri ravne linije oblike konvergentnega profila Lavalove šobe so dosegli višje temperature delcev v primerjavi z Lavalovo šobo, ki je imela Vitosinskejeve krivulje ukrivljenosti. Čas zadrževanja delcev v primeru ravne linije konvergentnega profila Lavalove šobe je bil daljši kot pri Lavalovi šobi z ukrivljenostjo po Vitosinskem. Po drugi strani pa so ugotovili, da vstopna dolžina konvergentnega dela šobe očitno vpliva na temperaturo delcev in čas zadrževanja delcev, ki je naraščal s povečevanjem dolžine konvergentnega profila. Z analiziranjem stanja raztaljenih delcev in njihove hitrosti so lahko pri optimalni konfiguraciji šobe puške za naprševanje (0,7 V) napovedali izdelavo prevleke z majhno poroznostjo. Te izračune so tudi eksperimentalno potrdili z izdelavo nizko porozne amorfne prevleke (1,37 %) na osnovi železa pri računalniško napovedani optimalni konfiguraciji šobe za HVAF.

Ključne besede: amorfne prevleke na osnovi železa, postopek HVAF, računalniška simulacija, šoba

1 INTRODUCTION

Fe-based amorphous coatings (ACs) are promising for applications in the military and nuclear industry, oil and gas industry and manufacturing due to their excellent corrosion resistance, wear resistance and neutron-absorption ability.¹ The high-velocity air-fuel (HVAF) thermal spray technique is frequently used to fabricate Fe-based ACs.²⁻⁴ During a HVAF spray process, porosity defects in the coating are inevitable, significantly influencing the corrosion behavior.⁵ In the HVAF spray process, both the particle temperature and particle velocity attained in flight are the determining factors for porosity defects. The particle heating and ac-

celeration can be efficiently controlled by changing the Laval-nozzle geometry. Therefore, the Laval nozzle is an important part of a HVAF thermal spray gun, affecting the quality of the coating.

Nowadays, the nozzle gun used for the HVAF thermal spray process is a Laval nozzle, which consists of a convergent section and a divergent section. The influence of the nozzle geometry on the thermal spray process was studied experimentally. The change in the entrance convergent section length of the gun nozzle had a significant effect on the deposition efficiency, microstructure, and hardness of the HVOF-sprayed $Al_2O_3-40\text{ w\% }TiO_2$ coatings.⁶ The effect of nozzle configuration on the performance of WC-based coatings was also studied experimentally. Matikainen et al.⁷ studied the effect of nozzle configuration on the tribological properties of HVAF-sprayed WC-CoCr coatings. Their results showed

*Corresponding author's e-mail:
wunianchu@163.com (Nianchu Wu)

that the particle melting and average particle velocity can be efficiently controlled by changing the nozzle geometry from cylindrical to convergent–divergent, resulting in an improvement in the density and microstructure of a coating. Lyphout et al.⁸ studied mechanical and wear properties of WC-CoCr coatings for different nozzles varying in length. Their results showed that increasing the length of a nozzle leads to an improvement in the microhardness and abrasion wear resistance of a coating. In another study by Kumar et al.,⁹ it was shown that the AK06 HVOF gun with different nozzle configurations can also change average particle velocities. The effect of nozzle configuration on the deposition, microstructural features, hardness and sliding wear behavior of HVOF-sprayed WC-CoCr coatings was evaluated. Fine and coarse feedstock powders were found to be sensitive to the type of nozzle used, while no major difference was observed in the coatings from powders with a medium size sprayed with different nozzles.¹⁰ Among all of the above studies, none studies the influence of the nozzle configuration effect on the quality of Fe-based ACs.

The nozzle geometry, which influences the combustion gas dynamics, is one of the most important parameters in a thermal spray process. To date, the influence of the nozzle configuration on a thermal spray process has

been investigated by computational fluid dynamics simulations. Numerical simulation has investigated the effect of increasing the throat diameter and the nozzle entrance converging section on the HVOF-sprayed Al₂O₃–40 wt% TiO₂ coatings. When increasing the entrance convergent section length of a nozzle, the particle temperature increases, but the particle velocity slightly decreases.⁶ As the diameter of the nozzle throat is increased, the location of the Mach shock disc moves backward from the nozzle exit into the HVOF system.^{11,12} Recently, for the WC-12Co coatings deposited by a HVOF spray process, it has been further found that a reduction in the Laval nozzle throat diameter increases the particle velocity and does not obviously affect the particle temperature. A reduced Laval nozzle divergent angle causes an increase in the particle temperature and velocity. The longer the length of the Laval nozzle divergent part, the higher is the temperature of the particles.¹³ However, only few studies have focused on the convergent-section geometry (the length and curve shape) of the gun nozzle design for HVOF-sprayed Fe-based ACs to improve their density and properties. The shape of the convergent curve affects the uniformity of the nozzle outlet airflow and a good convergent part can improve the stability and uniformity, reducing the turbulence of the flow field. Therefore, it is necessary to design the shape and size of the convergent section geometry of the gun nozzle for a HVOF spray process in order to gain high-density Fe-based ACs.

In this research, the effect of the convergent section geometry of a gun nozzle on the characteristics of the flame flow and in-flight Fe-based amorphous particles during HVOF spraying was studied using CFD simulations. The convergent section geometry of a gun nozzle includes the nozzle entrance convergent section length and shape of the Laval nozzle convergent section (a straight line and Vitosinski convergence curve). Using the optimal gun configuration, predicted via this simulation, a Fe-based AC with a low porosity was fabricated during a HVOF thermal spray process.

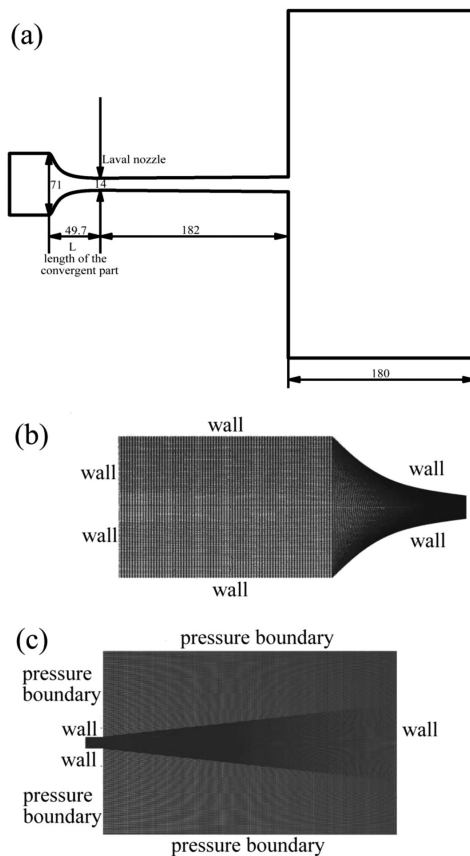


Figure 1: a) Schematic diagram of the AK07 spray gun with computational grid and boundary conditions used in the HVOF model; b) internal domain, including the combustion chamber and the convergent-divergent nozzle, c) external domain

2 MATHEMATICAL MODELING

2.1 Boundary conditions and grid meshing

Figure 1 shows the detailed mesh of an AK07 spray gun. Numerical methods and mathematical models were applied to the propane-fueled 2-D geometry. There are 85 680 cells and 86 664 nodes in the whole domain. The sensitive area grid, including the free jet region, air-fuel inlet, and the grids around the nozzle, has been successively refined to accurately capture the characteristics of the flame flow. The Laval nozzle geometric parameters can be varied in the following two aspects:

- 1) the length of the Laval nozzle convergent section,
- 2) the curve shape of the Laval nozzle convergent section.

Table 1 shows the spray parameters for HVOF-sprayed Fe-based ACs. **Table 2** lists six different lengths

Table 1: HVAF spray parameters for Fe-based ACs

Air pressure (kPa)	Propane pressure (kPa)	Nitrogen pressure (kPa)	Chamber pressure (kPa)	Feed rate (g/min)	Traverse velocity (mm/s)	Spray distance (mm)	Particle size (μm)
623.286	653.622	524.001	512.280	30	500	180	20–30

of the Laval nozzle convergent section and two kinds of shape of the Laval nozzle convergent section (a straight line and Vitosinski convergence curve), which are divided into eight cases for calculation and discussion. Particles in a size-range of 10–50 μm are injected into the nozzle. The physical properties of the Fe-based amorphous powder can be given as follows: $\rho = 7701 \text{ kg/m}^3$ and $C = 680.5 \text{ J/(kg}\cdot\text{K)}$. The walls of the spray gun are all assumed to be at a constant temperature of 300 K. The pressure far field and pressure outlet boundary are applied at the external domain. Finally, the atmospheric pressure is assumed to be 1010 Pa.

Table 2: Different lengths (L) of the Laval nozzle convergent part and shape of the Laval nozzle convergent part for HVAF thermal spray Fe-based ACs

Case	Variable	
	Length (mm)	Shape
0.4-S	28	Straight line
0.4-V		Vitosinski convergence curve
0.6-S	42.6	Straight line
0.6-V		Vitosinski convergence curve
0.7-S	49.7	Straight line
0.7-V		Vitosinski convergence curve
0.8-S	56.8	Straight line
0.8-V		Vitosinski convergence curve

2.2 Gas-flow model

The "realizable $k-\epsilon$ model" is used extensively in the HVAF simulation. The governing equations for the 2-D model in the Cartesian tensor are defined below:¹⁴

Mass conservation Equation (1):

$$\frac{\partial \rho}{\partial t} + \frac{\partial}{\partial x_i}(\rho v_i) = 0 \quad (1)$$

Momentum conservation Equation (2):

$$\begin{aligned} \frac{\partial}{\partial t}(\rho v_i) + \frac{\partial}{\partial x_j}(\rho v_i v_j) = \\ = \frac{\partial \pi}{\partial x_i} + \frac{\partial}{\partial x_j}(\tau_{ij})_{\text{eff}} + \frac{\partial}{\partial x_j}(\rho v_i \bar{v}_j) \end{aligned} \quad (2)$$

Energy transport Equations (3) and (4):

$$\begin{aligned} \frac{\partial}{\partial t}(\rho E) + \frac{\partial}{\partial x_i}[v_i(\rho H + p)] = \\ = \frac{\partial}{\partial x_j} \left(k_{\text{eff}} \frac{\partial T}{\partial x_j} + v_i(\tau_{ij})_{\text{eff}} \right) + S_h \end{aligned} \quad (3)$$

$$(\tau_{ij})_{\text{eff}} = \mu_{\text{eff}} \left(\frac{\partial v_j}{\partial x_i} + \frac{\partial v_i}{\partial x_j} \right) - \frac{2}{3} \mu_{\text{eff}} \frac{\partial v_i}{\partial x_i} \delta_{ij} \quad (4)$$

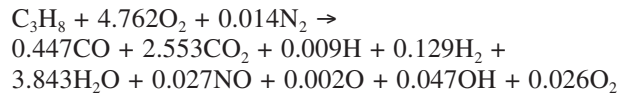
Effective thermal conductivity Equation (5):

$$k_{\text{eff}} = k + \frac{c_p \mu_t}{\sigma_t} \quad (5)$$

where x_i is the coordinate in the i direction, v is the velocity, i and j are the coordinate indices, v_i is the velocity in the i -direction, ρ is the density, τ_{ij} is the deviatoric stress tensor, H is the enthalpy, p is the particle, k_{eff} is the effective thermal conductivity, T is the temperature, S_h is the chemical reaction source energy, μ is the viscosity, δ is the Kronecker symbol, C_p is the specific heat of the particle.

2.3 Combustion model

In practice, the chemical reactions between hydrocarbon and air in the HVAF chamber are extremely complex, not only because they consist of a large number of elementary reactions, but also because the combustion products may decompose at high temperature and pressure due to the strong thermal vibration of atoms.¹⁵ Therefore, it is necessary to simplify the chemical reactions in the combustion chamber. In this study, the chemical equilibrium code developed by Gorden and McBride is used to calculate the stoichiometry of each product. The chemical reaction considered in our model is as follows:



An eddy dissipation model is used to solve this global reaction. This approach is based on the solution of transport equations for species mass fractions. The reaction rates are assumed to be controlled with the turbulence rather than a calculation of the Arrhenius chemical kinetics. The net rate of production for species i due to reaction r is given by the smaller of Equations (6) and (7) below:

$$R_{i,r} = v_{i,r} M_{\omega,i} A \rho \frac{\epsilon}{k} \min \left(\frac{Y_R}{v_{R,r} M_{\omega,R}} \right) \quad (6)$$

$$R_{i,r} = v_{i,r} M_{\omega,i} A B \rho \frac{\epsilon}{k} \min \left(\frac{\sum_P Y_P}{\sum_j v_{j,r} M_{\omega,j}} \right) \quad (7)$$

2.4 Particle models

The gas is treated as a continuum phase by solving the Navier-Stokes equations, while the dispersed particle phase is solved by tracking a large number of droplets. The trajectories of these discrete phase entities are computed in addition to the heat and mass transfer to the gas phase.

The equation of motion for the particles in the x direction (using Cartesian coordinates) can be written as a force balance that equates the droplet inertia with the forces acting on the particle. The basic equations for a particle are Equations (8) and (9).¹⁶

$$\frac{dv_p}{dt} = \frac{18\mu}{\rho_p d_p^2} \frac{C_D Re}{24} (v - v_p) + a \quad (8)$$

The energy equation for a single particle, neglecting the heat transfer via radiation, is as follows:¹⁷

$$m_p c_p \frac{dT_p}{dt} = kA_p (T_g - T_p) \quad (9)$$

where v_p is the particle velocity, d_p is the particle diameter, C_D is the drag coefficient, Re is the Reynolds number, a is the acceleration, m_p is the mass of the particle, T_p is the particle temperature, k is the coefficient of heat transfer, A_p is the surface area of the particle, T_g is the gas temperature. The density of a Ni-based amorphous alloy is 8200 kg/m^3 and the specific heat is $400 \text{ J/(kg}\cdot\text{K)}$.

3 EXPERIMENTAL PART

The Fe-based AC composition is (Fe 54.5, Cr 18.4, Mn 2, Mo 13.9, W 5.8, B 3.2, C 0.9 and Si 1.3) *w*%. A 316 stainless steel plate with dimensions of $(100 \times 50 \times 5) \text{ mm}$ was used as the substrate. The Fe-based AC was fabricated using an AK07 HVAF thermal spray system from Kermetico Company. Detailed spraying parameters for the HVAF process are shown in **Table 1**.

The microstructure of the powders and coatings were examined with SEM (Quanta 600). An X-ray diffraction (XRD) analysis of the powders and coatings was conducted on a Rigaku D/max 2400 diffractometer (Tokyo, Japan) with monochromated $\text{Cu-K}\alpha$ radiation. Porosity can be easily detected with SEM micrographs during an image analysis due to a high degree of contrast between the dark pores and more highly reflective coating material. Porosity was evaluated by analyzing the SEM micrographs with the Image-Pro-Plus 6.0 software.

4 RESULTS AND DISCUSSION

4.1 Gas dynamics for different Laval-nozzle convergent-section designs

Simulated contours of the pressure, velocity magnitude and temperature in both the internal and external

fields for different gun configurations from **Table 2** (0.4 S, 0.6 S, 0.7 S, 0.8 S, 0.4 V, 0.6 V, 0.7 V, 0.8 V) are shown in **Figures 2–4**. In order to investigate the gas-flow characteristics, the distributions of pressure, velocity and temperature at the center line of the HVAF thermal spray gun for different gun configurations (0.4 S, 0.6 S, 0.7 S, 0.8 S, 0.4 V, 0.6 V, 0.7 V, 0.8 V) are shown in **Figures 5 and 6**. The air and propane are injected into the combustion chamber, undergoing a chemical reaction. The high-pressure gas flow through the constrained nozzle gives rise to a supersonic flame flow. As the thermal energy generated by combustion is converted into kinetic energy through the convergent–divergent nozzle, the high pressure in the combustion chamber decreases continuously. The fluctuations in the flame pressure at the barrel exit are created periodically by the overexpanding flow, subsequently re-converging above and below the atmospheric pressure.¹⁸ The velocity at the throat can reach the velocity of sound, and at the exit of the divergent section it reaches two times the velocity of sound. Four diamond waves appear at the nozzle exit, which then gradually decay until they disappear. In addition, the gas temperature increases sharply within the

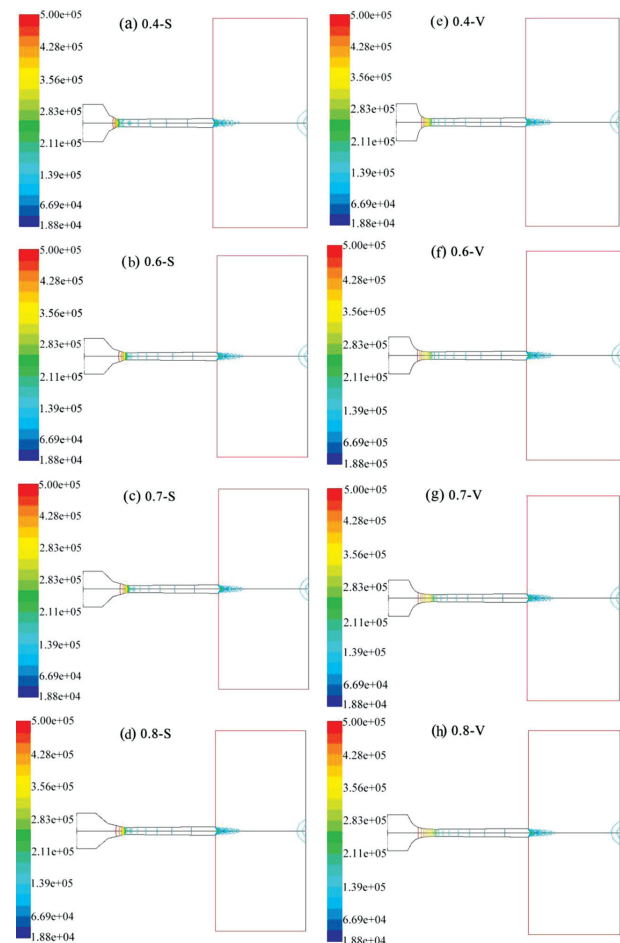


Figure 2: Calculated contours of the gas pressure for different gun configurations

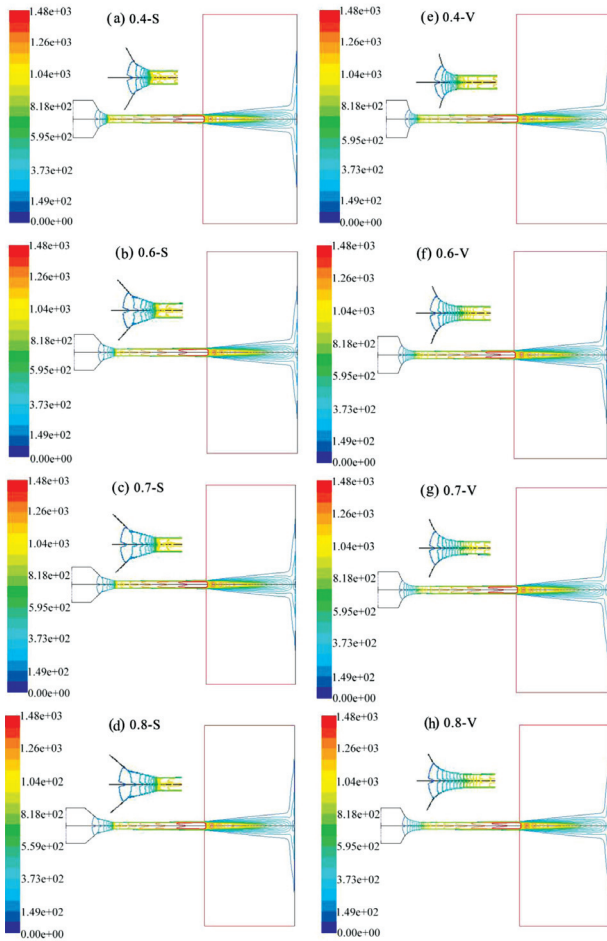


Figure 3: Calculated contours of the gas velocity magnitude for different gun configurations and insets showing the convergent section of the nozzle gun

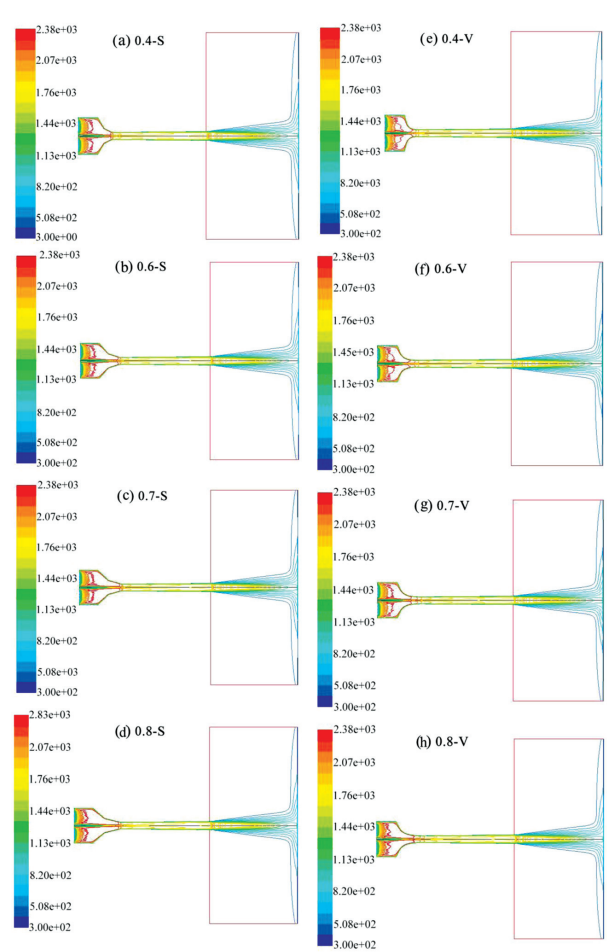


Figure 4: Calculated contours of the gas temperature for different gun configurations

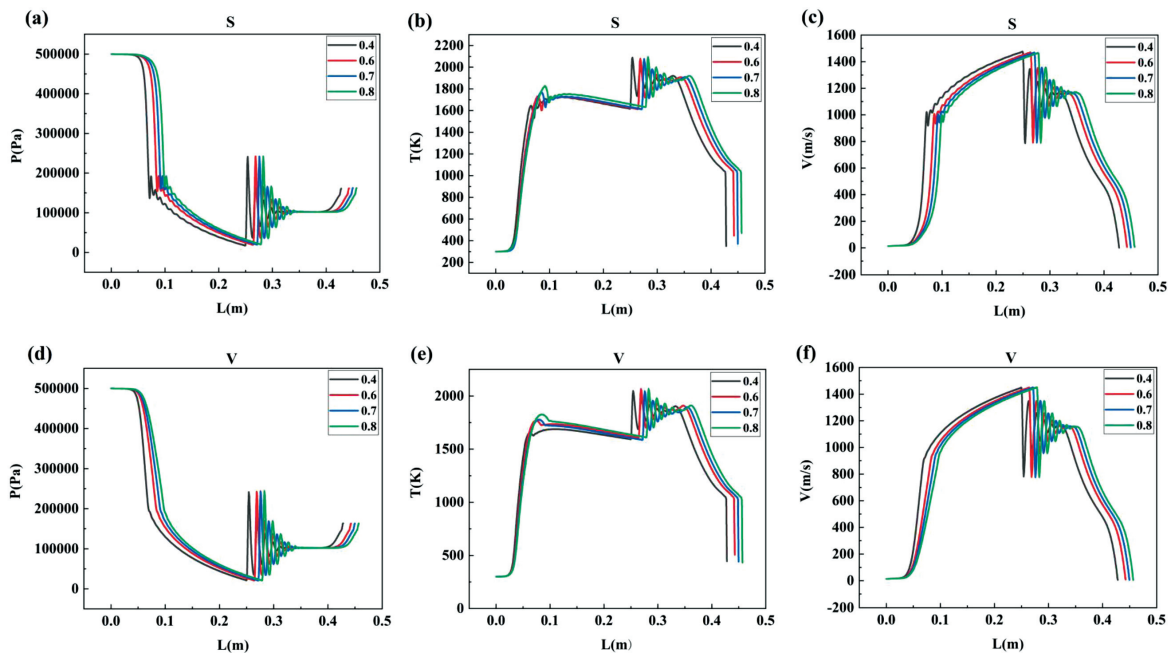


Figure 5: Calculated contours of the flame and gas characteristics along the centerline for the nozzle entrance convergent section length: a) and d) gas pressure, b) and e) gas temperature, c) and f) gas velocity

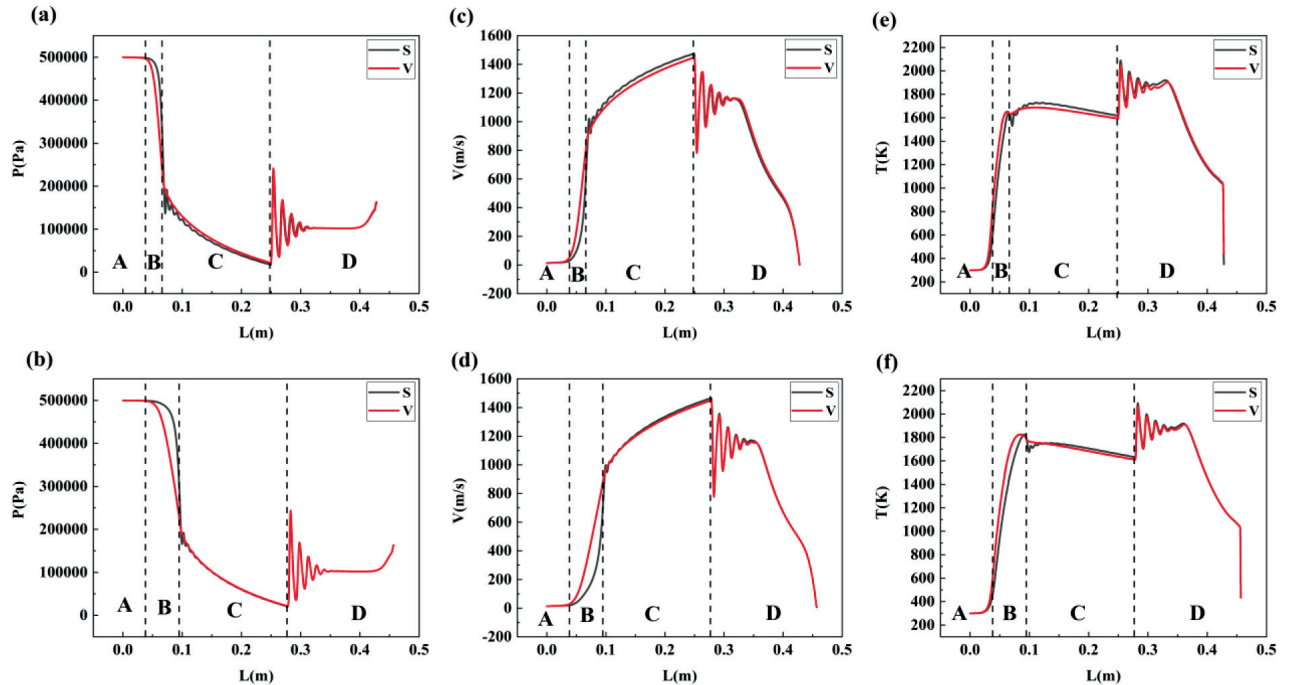


Figure 6: Calculated contours of the flame and gas characteristics along the centerline of the Laval nozzle convergent straight line and Vitosinski convergence curve: a) and b) gas pressure, c) and d) gas velocity, e) and f) gas temperature

combustion nozzle and reaches its peak near the exit of the nozzle. There are four noticeable hollow circles in the core of the free jet. The temperature curve shows damping oscillation.

Below we discuss the effect of the increasing convergent section length of the nozzle on the gas flame flow characteristics. As shown in **Figure 6**, there are four sections of the HVOF thermal spray process, that is, the chamber (A), the convergent section (B), the divergent section (C) and the atmosphere (D). The length of the convergent part (ranging from 28 mm to 56.8 mm) has no effect on the initial chamber pressure, gas velocity and temperature. And with the increasing length of the convergent part, the location of the Mach shock disc moves backward from the nozzle exit (see **Figure 5**). There are shock waves of equal magnitude at the gun outlet as the length of the convergent part is increasing.

Next, the effect of the shape (a straight line or Vitosinski curve) of the nozzle on the gas flame flow characteristics is discussed. The Vitosinski-curve variation is smoother than that of the straight line. Consequently the change in the gas flame flow characteristics (pressure, velocity and temperature) for the Vitosinski curve shows a uniform and stable flame compared with the straight-line curve (see **Figures 3** and **6**) in the convergent section. In addition, we can see that the Vitosinski curve falls flat at the throat after a sharp decline. For the Vitosinski curve, the diameter gradient at the far end of the throat is larger than that of the nozzle, while the radius change at the front part of the convergent section is relatively flat. However, the gas velocity and temperature increase a little for the nozzle with a straight-line curve

compared with those of the nozzle with a Vitosinski curve. Meanwhile, the effect of the increasing nozzle entrance convergent section length on the gas flame flow characteristics is also discussed. The gas pressure, velocity and temperature remain the same when the HVOF nozzle entrance convergent section length ranges from 28 mm to 56.8 mm (see **Figure 5**).

4.2 Effect of the Laval nozzle convergent section design on the particle velocity and temperature

Numerical simulation results on the effect of the increasing nozzle entrance convergent section length (from 28 mm to 56.8 mm) on the particle velocity and particle temperature for the same particle sizes (10 μm and 50 μm) and two kinds of curve shape of the Laval nozzle convergent section (a straight line and Vitosinski convergence curve) are given in **Figures 7** and **8**, respectively. The results show that the particle velocity for the straight line and Vitosinski convergence curve increases slightly with the increasing nozzle entrance convergent section length. That is, the change in the nozzle convergent section length has a weaker effect on the particle velocity. However, as shown in **Figure 8**, the increasing nozzle entrance convergent section length leads to a significant increase in the axial particle temperature for particle sizes of 10 μm and 50 μm . When the nozzle entrance convergent section length increases from 28 mm to 56.8 mm, the increased amplitude of the particle temperature is about 200 K. The reason for this is the fact that the particles stay in the flame flow for a longer time to gain more heat. Therefore, the particle velocity and tem-

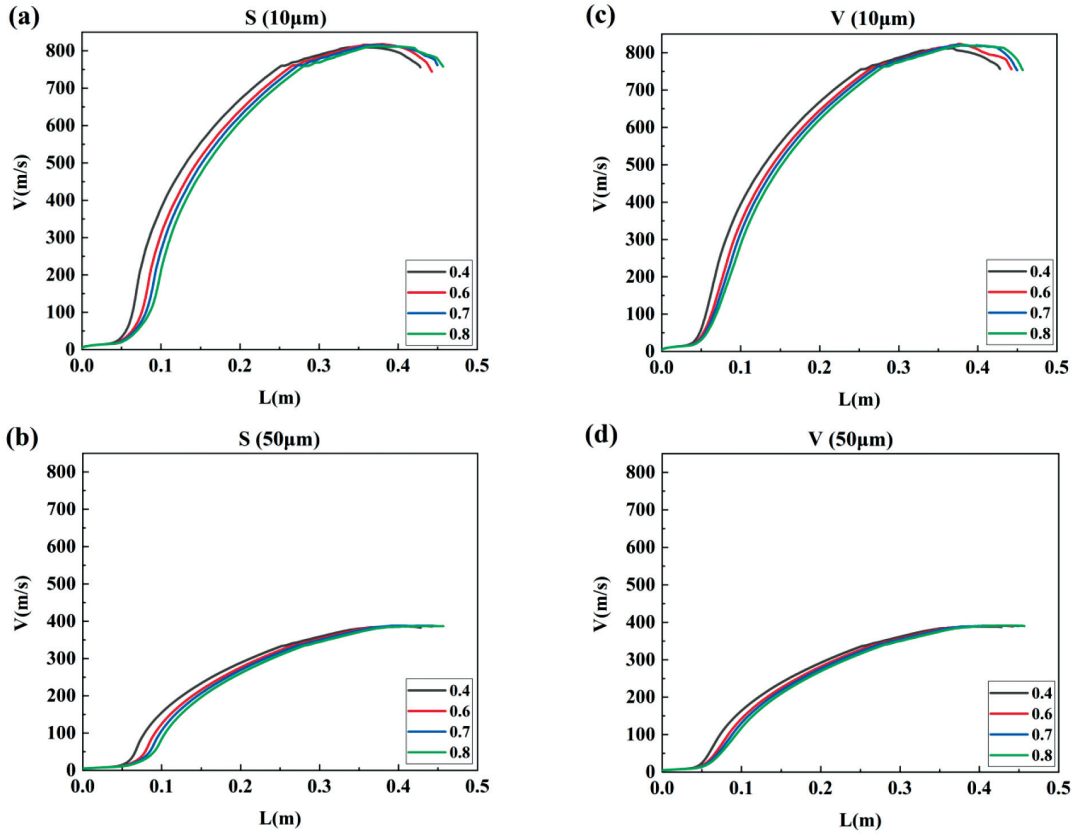


Figure 7: Predicted particle axial velocity for the nozzle entrance convergent section length

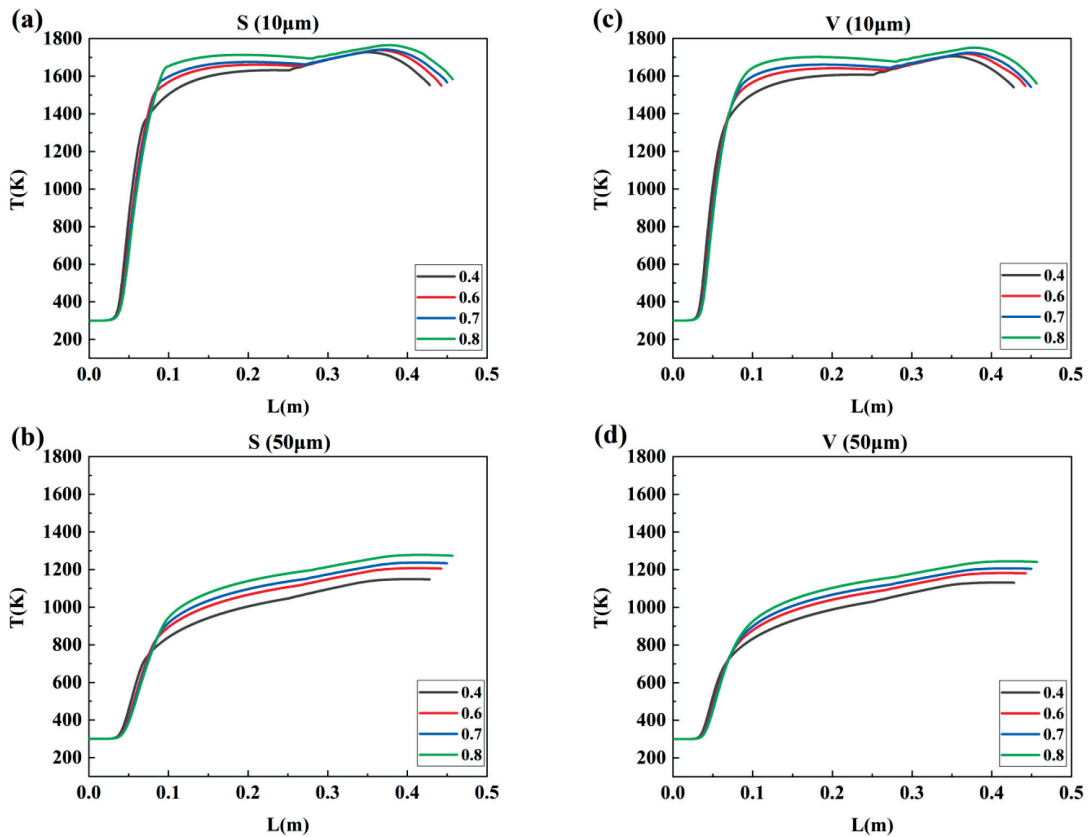


Figure 8: Predicted particle axial temperature for the nozzle entrance convergent section length

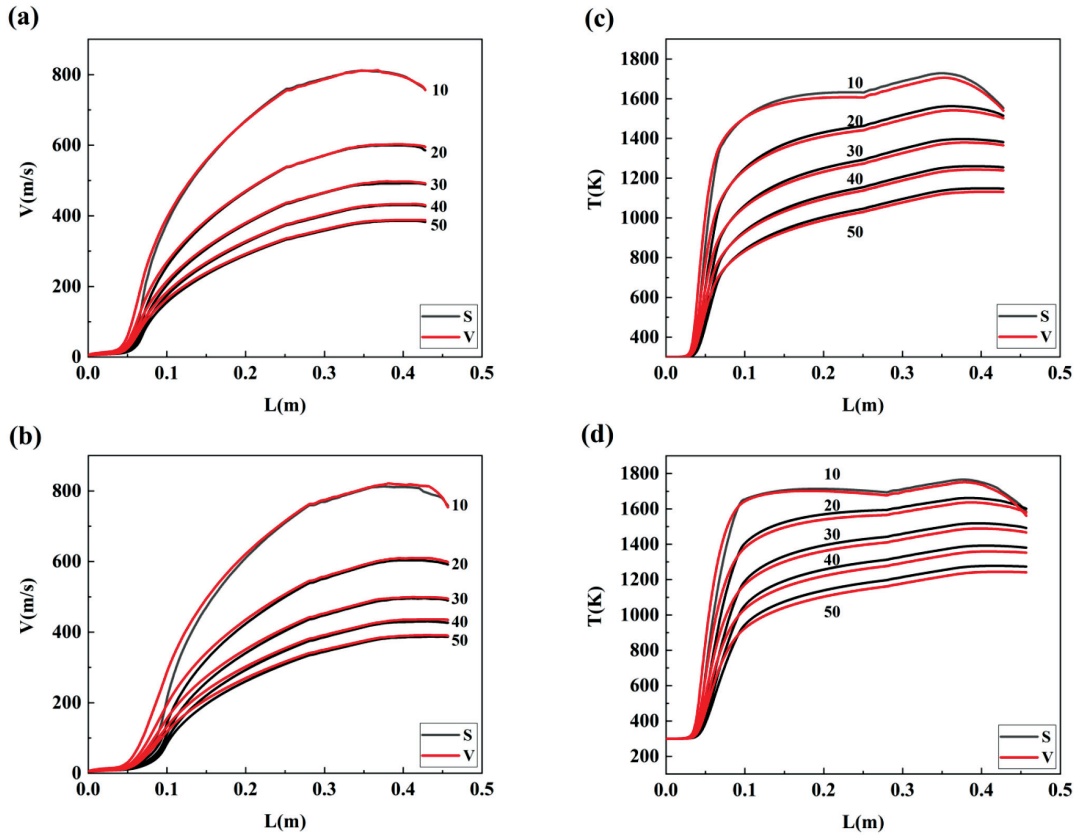


Figure 9: Predicted values for different curve shapes of the Laval nozzle convergent sections and particle sizes: a) and b) particle axial velocity, c) and d) temperature

perature impacting the substrate can be adjusted by changing the nozzle entrance convergent section length.

Figure 9 illustrates the particle velocity and temperature curves for the centerline with different shapes of the Laval nozzle convergent section (a straight line and Vitosinski convergence curve) and the same particle sizes (10 μm and 50 μm). In **Figures 9a** and **9b**, the particle velocity for the Vitosinski curve shape of the Laval nozzle convergent section is a little higher than that for the straight-line curve shape of the Laval nozzle convergent section. In contrast, compared with the Vitosinski curve shape of the Laval nozzle convergent section, the straight-line shape of the Laval nozzle convergent section has a higher particle temperature (see **Figures 9c** and **9d**). Thus, compared with the nozzle entrance convergent section length, the curve shape of the Laval nozzle convergent section has a weaker effect on the particle velocity and temperature.

4.3 Particle melting behavior for different Laval nozzle convergent section designs

In the HVAF spray process, an increase in the particle temperature and in-flight velocity is not always beneficial for the deposition of particles. And more important, it is related to the melt status of the particles. The melting index (*MI*) is used to characterize the melt status of the particles. *MI* is defined as the ratio of the dwell time

of particle to the time required to melt one in-flight particle, to indicate the molten state of a particle in a particle jet. A higher *MI* signifies a better melt status. A low *MI* reflects partial melt or unmelted conditions. A *MI* calculation is presented in Equation (10):

$$MI = \frac{24k}{\rho h_{fg}} \cdot \frac{1}{1 + 4/Bi} \cdot \frac{(T_s - T_m) \cdot \Delta t_{fly}}{d^2} \quad (10)$$

where T_s is the particle temperature, T_m is the particle melting point (1 404 K), k is the thermal conductivity of liquid (40 W/(m·K⁻¹), h_{fg} is the latent heat (26 7000 J/Kg), Bi is the Biot number defined as hd/k where d is the particle diameter (30 μm), h is the heat transfer coefficient (6 000 J/Kg), Δt_{fly} is the particle dwell time and v is the particle velocity. The particle velocity and particle temperature can be observed in **Figures 7** and **8**. **Figure 10** shows the particle dwell time (Δt_{fly}) along the centerline for different shapes of the Laval nozzle convergent section (a straight line and Vitosinski convergence curve) and the nozzle entrance convergent section length L (from 28–56.8 mm) for the same particle sizes (10 μm and 50 μm). It can be seen that the particle dwell time gradually increases with the increasing nozzle entrance convergent section length. And for the same nozzle entrance convergent section length, the particle dwell time for the straight-line shape of the Laval nozzle convergent section is longer than

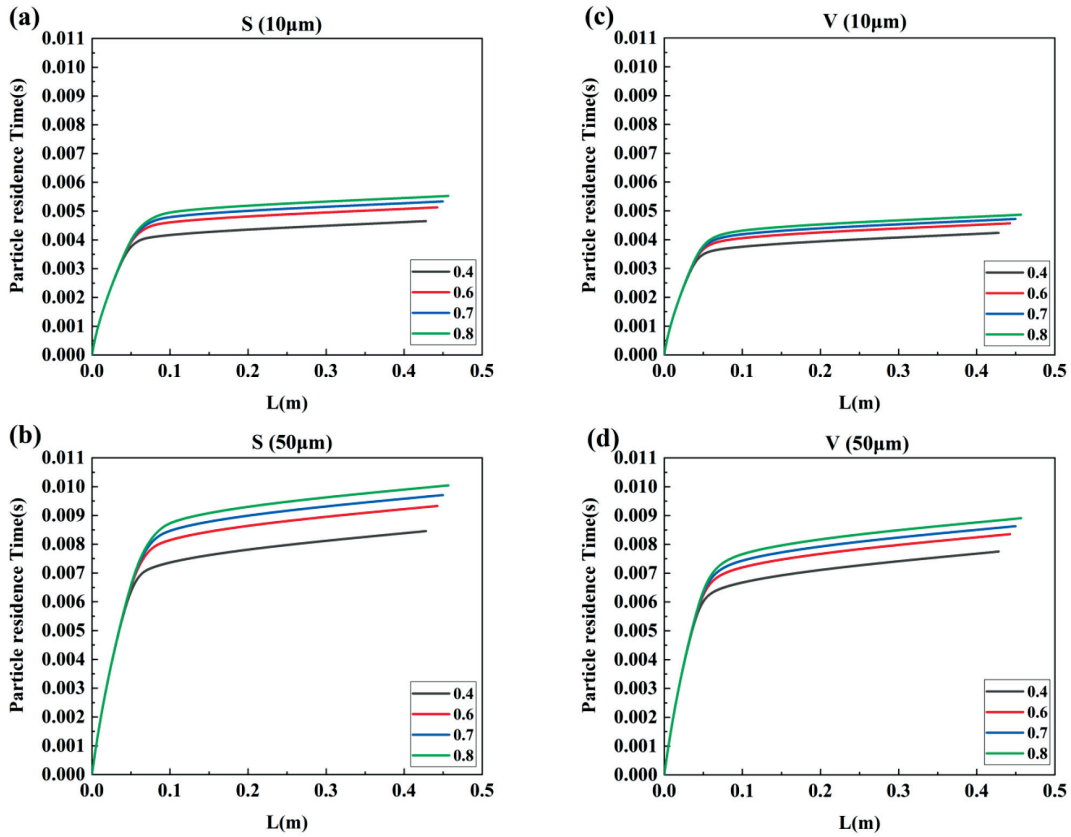


Figure 10: Particle dwell time along the centerline for different nozzle entrance convergent configurations (0.4 S, 0.8 S, 0.4 V, 0.8 V) and for particle sizes of 10 μm and 50 μm

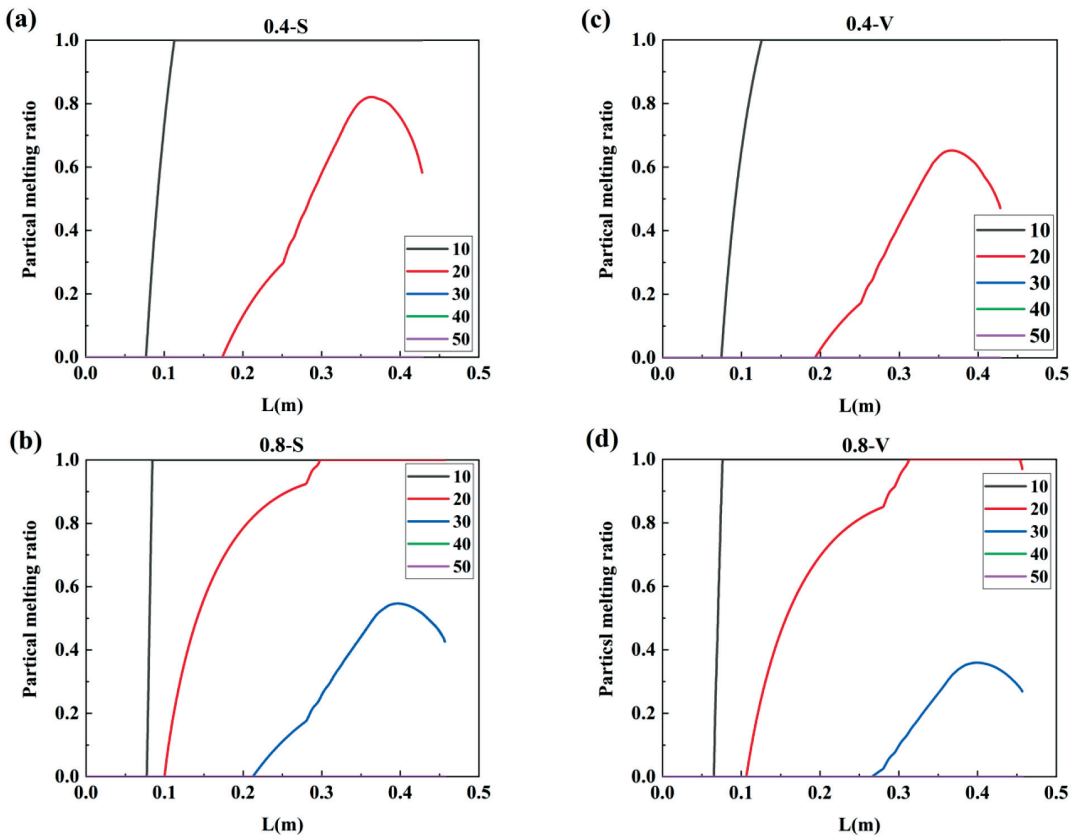


Figure 11: MI along the centerline for different nozzle entrance convergent configurations and for particle sizes of 10–50 μm

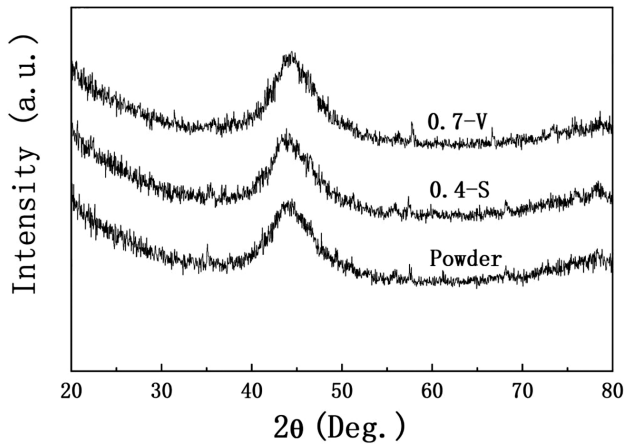


Figure 12: XRD patterns for the atomized powder and HVOF-sprayed ACs (0.4 S and 0.7 V configuration)

that for the Vitosinski-curve shape of the Laval nozzle convergent section.

To sum up, the MI along the centerline with different nozzle entrance convergent configurations (0.4 S, 0.8 S, 0.4 V, 0.8 V) for the same particle sizes (10 μm and 50 μm) can be observed in **Figure 11**. Particles of the large size (50 μm) may not reach the melting point, remaining in the solid state during the entire flight. Particles of the small size (10 μm) may be heated to the melting point in a short time and be fully melted during the flight, finally hitting the substrate in the solid state. When particles of a medium size (20 μm and 30 μm)

reach the substrate, they are in a semi-molten state (where both the liquid and solid coexist). Particles with the size of 20 μm are the first to melt completely and be eventually in the state of coexistence between the liquid and solid after a long enough distance. The melt status of the particles is the key to creating low porosity and dense coatings.^{19,20} The optimum thermal spraying occurs when the particles reach the substrate in a semi-molten state. It can be seen in **Figure 11** that the melt status of the particles for the nozzle entrance convergent configuration of 0.7 V and 0.6 S might be mostly a semi-molten state. It is clear that an increase in the particle velocity significantly improves the coating density. As shown in **Figure 7**, the particle velocity, impacting the nozzle entrance convergent configuration of 0.7 V is a little larger than the particle velocity, impacting the nozzle entrance convergent configuration of 0.6 S. Thus, we found that the optimal nozzle entrance convergent configuration for the Fe-based ACs is 0.7 V.

4.4 Experimental validation

To validate the simulations, Fe-based amorphous coatings were fabricated using powders and two gun configurations (0.7 V, 0.4 S). The XRD patterns of the atomized powder and the as-deposited coatings for each gun configuration (0.7 V, 0.4 S) are shown in **Figure 12**. The diffuse pattern and the absence of any peaks associated with crystalline phases indicate that they are fully amorphous. The structures of cross-sections and the sur-

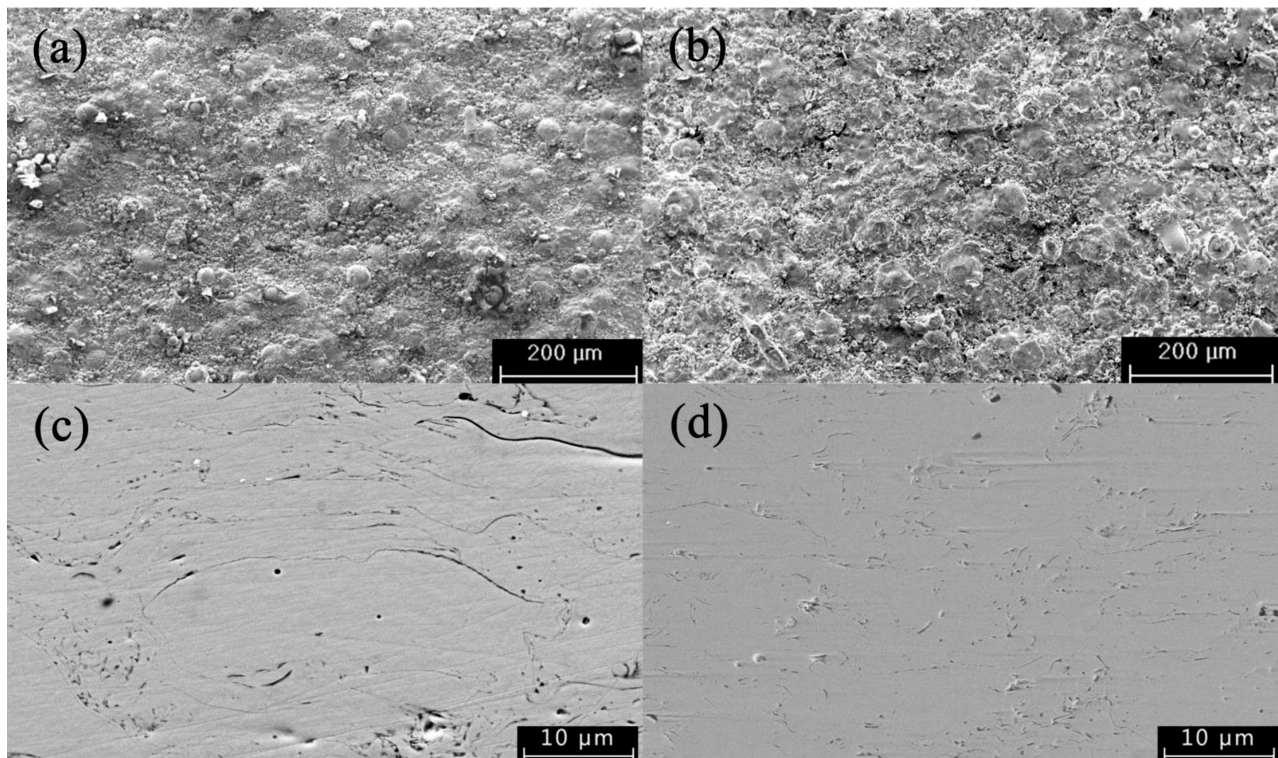


Figure 13: SEM micrographs of the HVOF coatings for 0.4 S and 0.7 V gun configuration: a) and b) as-sprayed surface, c) and d) cross-section

face morphologies of different Fe-based ACs are shown in **Figure 13**. The surface morphology reveals that with the gun configuration of 0.4 S the powder was not fully melted during spraying (**Figure 12a**). Thus, the porosity of the coating applied at the gun configuration of 0.4 S is 2.71 % (**Figure 12c**). However, the coating applied at the gun configuration of 0.7 V was almost fully melted (see **Figures 12b** and **12d**). An almost fully dense coating with a porosity of approximately 1.37 % was obtained at the gun configuration of 0.7 S, which is lower than that for the gun configuration of 0.4 S. Thus, dense Fe-based AMs can be obtained using the gun configuration of 0.7 V.

5 CONCLUSIONS

The effect of the convergent section geometry of a gun nozzle on the HVAF thermal spray Fe-based AC process was investigated using predictive simulations and verified via an experiment. CFD was used to investigate the gas-flow field and the behavior of in-flight particles at the nozzle entrance convergent section length ranging from 28 mm to 56.8 mm and different shapes of the Laval nozzle convergent section (a straight line and Vitosinski convergence curve). The main findings are summarized as follows:

1) For the gas-flow field, the length of the convergent part (ranging from 28 mm to 56.8 mm) does not affect the initial chamber pressure, gas velocity or temperature. The change in the gas flame flow characteristics at the Vitosinski curve shows a uniform and stable flame compared with the straight line of the convergent section. In addition, the gas velocity and temperature increase slightly more for the nozzle with a straight-line curve than for the nozzle with a Vitosinski curve.

2) For the in-flight flow field, the change in the nozzle convergent section length has a weaker effect on the particle velocity. However, the nozzle entrance convergent section length leads to a significant increase in the axial particle temperature. That is, the longer the length of the nozzle entrance convergent section, the higher is the particle temperature. The particle velocity at the Vitosinski-curve shape of the Laval nozzle convergent section is a little higher than that at the straight-line shape of the Laval nozzle convergent section. And the straight-line shape of the Laval nozzle convergent section causes a higher particle temperature compared with the Vitosinski-curve shape of the Laval nozzle convergent section. In addition, the particle dwell time increases with the increasing nozzle entrance convergent section length, and the particle dwell time at the straight-line shape of the Laval nozzle convergent section is higher than that at the Vitosinski-curve shape of the Laval nozzle convergent section.

3) The optimal nozzle entrance convergent configuration is 0.7 V because the melt status of the particles is a mostly semi-molten state and the particle velocity at im-

pact is high. Using this optimized gun configuration (0.7 V), we obtained low-porosity (1.37 %) Fe-based ACs.

Acknowledgements

This work was supported by the Natural Science Foundation of Liaoning Province under Grant No. 2022-MS-364, Educational Commission of Liaoning Province of China under Grant No. L202002, and Fushun Revitalization Talents Program under Grant No. FSYC202107011.

6 REFERENCES

- ¹ K. S. Nayak, A. Kumarb, T. Laha, Fe-based metallic glass coatings by thermal spraying: a focused review on corrosion properties and related degradation mechanisms, *International Materials Reviews*, (2022), doi:10.1080/09506608.2022.2084670
- ² B. Huang, C. Zhang, G. Zhang, H. L. Liao, Wear and corrosion resistant performance of thermal-sprayed Fe-based amorphous coatings, *Surface and Coatings Technology*, 377 (2019), 124896, doi:10.1016/j.surfcoat.2019.124896
- ³ X. Liu, Y. Wu, Z. Qiu, Z. Lu, S. Yao, S. Zhuo, D. Zeng, Simultaneously enhancing wear and corrosion resistance of HVAF-sprayed Fe-based amorphous coating from Mo clad feedstock, *Mater. Process. Technol.*, 302 (2022), 117465, doi:10.1016/J.JMATPROTEC.2021.117465
- ⁴ E. Sadeghi, S. Joshi, Chlorine-induced high-temperature corrosion and erosion-corrosion of HVAF and HVOF-sprayed amorphous Fe-based coating, *Surf. Coating. Technol.*, 371 (2019), 20–35, doi:10.1016/j.surfcoat.2019.01.080
- ⁵ N. Ahmed, M. S. Bakare, D. G. McCartney, K. T. Voisey, The effects of microstructural features on the performance gap in corrosion resistance between bulk and HVOF sprayed Inconel 625, *Surf. Coat. Technol.*, 204 (2010), 2294–2301, doi:10.1016/j.surfcoat.2009.12.028
- ⁶ K. Sakaki, Y. Shimizu, Effect of the Increase in the Entrance Convergent Section Length of the Gun Nozzle on the High-Velocity Oxygen Fuel and Cold Spray Process, *Journal of Thermal Spray Technology*, 10 (2001), 487–496, doi:10.1361/105996301770349268
- ⁷ V. Matikainen, H. Koivuluoto, P. Vuoristo, J. Schubert, Š. Houdkova, Effect of nozzle geometry on the microstructure and properties of HVAF-sprayed WC-10Co4Cr and Cr3C2-25NiCr coatings, *J. Therm. Spray Technol.*, 27 (2018), 680–694, doi:10.1007/s11666-018-0717-z
- ⁸ C. Lyphout, S. Bjorklund, M. Karlsson, M. Runte, G. Reisel, P. Boccaccio, Screening design of supersonic air fuel processing for hard metal coatings, *J. Therm. Spray Technol.*, 23 (2014), 1323–1332, doi:10.1007/s11666-014-0139-5
- ⁹ R. K. Kumar, M. Kamaraj, S. Seetharamu, T. Pramod, P. Sampathkumaran, Effect of spray particle velocity on cavitation erosion resistance characteristics of HVOF and HVAF processed 86WC-10Co4Cr hydro turbine coatings, *J. Therm. Spray Technol.*, 25 (2016), 1217–1230, doi:10.1007/s11666-016-0427-3
- ¹⁰ K. Torkashvand, M. Gupta, S. Bjorklund, F. Marra, L. Baiamonte, S. Joshi, Influence of nozzle configuration and particle size on characteristics and sliding wear behaviour of HVAF-sprayed WC-CoCr coatings, *Surface & Coatings Technology*, 423 (2021), 127585, doi:10.1016/j.surfcoat.2021.127585
- ¹¹ S. H. Kim, Y. J. Kim, Flow characteristics in compact thermal spray coating systems with minimum length nozzle, *Plasma Science and Technology*, 550 (2009), doi:10.1088/1009-0630/11/5/07
- ¹² J. S. Sang, Y. J. Kim, Effect of nozzle shape on the performance of high velocity oxygen-fuel thermal spray system, *Surface & Coatings*

- Technology, 202 (2008), 5457–5462, doi:10.1016/j.surfcoat.2008.06.061
- ¹³ X. Gao, C. Li, D. Zhang, H. X. Gao, X. Han, Numerical analysis of the activated combustion high-velocity air-fuel (AC-HVOF) thermal spray process: A survey on the parameters of operation and nozzle geometry, 405 (2021), 126588, doi:10.1016/j.surfcoat.2020.126588
- ¹⁴ S. Kamnis, S. Gu, Numerical modelling of propane combustion in a high velocity oxygen-fuel thermal spray gun, Chem. Eng. Process., 45 (2006), 246–253, doi:10.1016/j.cep.2005.06.011
- ¹⁵ D. Chang, Q. Xu, G. Trapaga, E. J. Lavernia, A numerical study of high-velocity oxygen fuel thermal spraying process. Part I: Gas phase dynamics, Metall. Mater. Trans. A, 32 (2001), 1609–1620, doi:10.1007/s11661-001-0139-1
- ¹⁶ H. Tabbara, S. Gu, Computational simulation of liquid-fuelled HVOF thermal spraying, Surf. Coat. Technol., 204 (2009), 676–684, doi:10.1016/j.surfcoat.2009.09005
- ¹⁷ M. H. Khan, T. Shamim, Investigation of a dual-stage high velocity oxygen fuel thermal spray system, Appl. Energy., 103 (2014), 853–862, doi:10.1016/j.apenergy.2014.03.075
- ¹⁸ H. Tabbara, S. Gu. A study of liquid droplet disintegration for the development of nanostructured coatings, J. Aiche., 11 (2012), 3533–3544, doi:10.1002/aic.13755
- ¹⁹ J. He, M. Ice, E. Lavernia, Particle melting behavior during high-velocity oxygen fuel thermal spraying, J. Therm. Spray Technol., 10 (2001), 83–93, doi:10.1361/105996301770349547
- ²⁰ J. A. Hearley, J. A. Little, J. A. Sturgeon, The effect of spray parameters on the properties of high velocity oxy-fuel NiAl intermetallic coatings, Surf. Coat. Technol., 123 (2000), 210–218, doi:10.1016/S0257-8972(99)00511-3